Launch of a sounding balloon for horizontal and vertical modeling of the ALAN propagation in the atmosphere

S. Cavazzani[1,2,3⋆], P. Fiorentin[4], C. Bettanini[4,6], M. Bartolomei[6], C. Bertolin[1], S. Ortolani[2,3], A. Bertolo[5], R. Binotto[5], L. Olivieri[6], A. Aboudan[6] and G. Colombatti[4]

[1] *NTNU, Department of Mechanical and Industrial Engineering, Gloshaugen, Richard Birkelands vei 2b, 7034, Trondheim, Norway*
[2] *Department of Physics and Astronomy, University of Padova, Vicolo dell'Osservatorio 3, 35122, Padova, Italy*
[3] *INAF-Osservatorio Astronomico di Padova, Vicolo dell'Osservatorio 5, 35122, Padova, Italy*
[4] *Department of Industrial Engineering, University of Padova, Via Gradenigo 6a, 35131, Padova, Italy*
[5] *Regional Environmental Prevention and Protection Agency of Veneto, Via Ospedale Civile 24, 35121, Padova, Italy*
[6] *CISAS - Center for Studies and Activities for Space Giuseppe Colombo, University of Padova, Via Venezia 15, Padova, Italy*

Accepted 2022 October 12. Received 2022 October 08; in original form 2022 July 31.

ABSTRACT

The propagation of light radiation in the atmosphere is a topic that needs to be properly analyzed to mitigate its negative influence on astronomical observation. This work describes a novel approach for evaluating atmospheric propagation of artificial light at night emphasizing (ALAN) the dependence on altitude and aerosols; it is based on an innovative experiment using a sounding balloon equipped with two sky quality meters (SQM): one vertically pointed at 30° (SQM-V) and the other horizontally at 90° (SQM-H) from the zenith. The system was launched during astronomical night condition from an area of the Italian Apennines with low ground light emission and crossed the Tuscan sky, observing the vertical and horizontal ALAN propagation. The data analysis of the two SQMs and their georeferentiation through altitude and trajectory reconstruction allows to model the propagation of light in the experiment field of view from few hundred meters up to an altitude of about 30 km. In this work main focus is given to the tropospheric part of atmosphere up to 12500 meters: the processed data is used to validate a theoretical model taking into account the altitude, the course of the balloon, the atmospheric composition and the population of the cities overflown by the balloon obtaining a correlation of 0.85 with the SQM-H and 0.91 with the SQM-V. The magnitude values close to 21.5 $mag \cdot arcsec^{-2}$ measured by the SQM-V at 2000 meters are an important experimental result for evaluating the influence of the aerosols and the altitude on the ALAN propagation.

Key words: sounding balloon – atmospheric effects – detectors – light pollution – site testing.

1 INTRODUCTION

Modeling of night sky brightness (NSB) propagation is an open and complex problem. The increase in artificial light at night (ALAN) led to the aggravation of light pollution. Light pollution is now widely and multidisciplinary studied (Kyba et al., 2015). In particular there are studies from various fields of astronomy (Patat et al., 2008; Puschnig et al., 2014; Zhang et al., 2016), ecology, biology (Holker et al., 2010; Gaston et al., 2013; Manfrin et al., 2017) and medicine (Kloog et al., 2009; Stevens et al. 2013). There is a rapidly growing literature on the subject (Mulder et al., 2015). There are two main contributions to NSB: the natural contribution, divided into terrestrial and extraterrestrial, and the artificial contribution (ALAN). ALAN is associated with several disorders, including increased incidence of cancer (Walker et al., 2020b), circadian rhythm disruption and mental health (Walker et al., 2020 and 2020a). ALAN has been detected to cause breast cancer, melatonin being the mediator between environment and the epigenome (Yang et al., 2015; Haim and Zubidat 2015). Night shifts combined with ALAN increase the risk of colorectal cancer in workers (Schernhammer et al., 2001; Walker et al., 2020b). ALAN not only adversely effects humans directly exposed to it, but it also affects the protected areas, undisturbed natural habitat of flora and fauna, vital to the human existence and well being (Aubrecht et al., 2010). This experiment has useful multidisciplinary implications, the results could implement the analysis of the ALAN impact on bird migration (Cabrera et al., 2018). Another highly topical scientific and multidisciplinary aspect is the analysis of the clouds and aerosol concentration and its influences on NSB, atmospheric conditions and human health (Shiraiwa et al., 2017). In this Paper we show the results of an innovative experiment to study this important phenomenon, in addition

⋆ E-mail:stefano.cavazzani@unipd.it

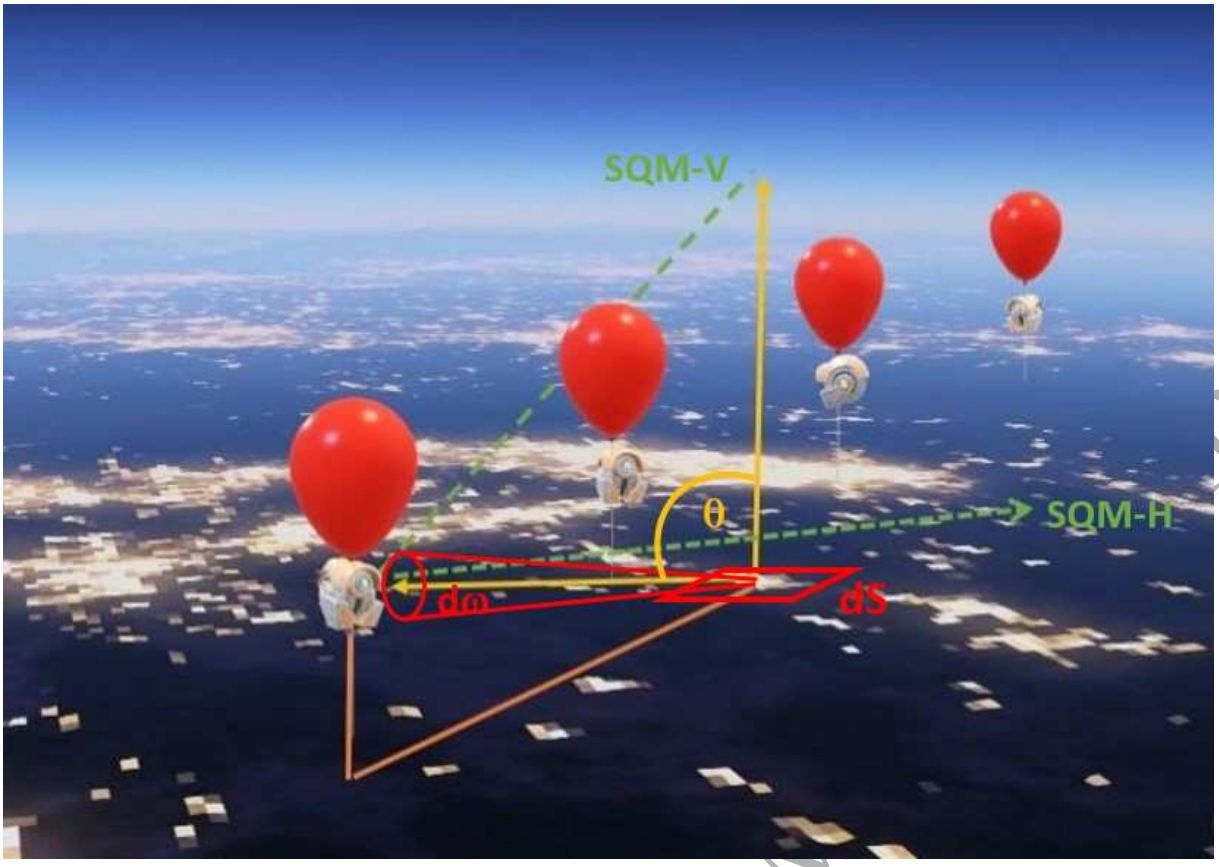

Figure 1. VIIRS image superimposed on the 3D geographical map of the experimental area: Tuscany region, Italy. Schematic representation of the analyzed balloon flight path, the dotted lines indicate the target of the two SQMs.

to our analysis, the data will also be useful for the implementation of the NSB study in relation to other scientific fields. The experimental area (Tuscany region, Italy) is also observed through the Visible Infrared Imaging Radiometer Suite (VIIRS) satellite data (see Figure 1). One of the aims of the work is the empirical validation of the NSB propagation model described in Cavazzani et al. (2020b). The model uses satellite data, the use of satellite for site testing is essential to reduce costs of ground-based campaigns and to increase the long-term trend. Satellites may have limits, but with careful analysis and correlation with ground data, even for limited periods, they can be calibrated and provide reliable results (Cavazzani et al. 2012, 2013, 2015, 2017 and 2019).

2 INSTRUMENTATION AND DATA DESCRIPTION

Figure 2 shows the configuration of the instrumentation used. In particular we see the two objectives of the sky quality meters (SQM): one at 30 degrees and the other at 90 degrees with respect to the zenith. The details of the instrumentation and balloon flight are published in Bettanini et al. (2022) and Fiorentin at al. (2019). The NSB measurements are performed with two Sky Quality Meter-Lens Ethernet (SQM-LE) mounted on the balloon, and the readings (every 1 second) at various observation temperatures are compensated with a temperature sensor. The spectral response of the SQM is between 350 and 700 nm, with maximum sensitivity between 500 and 550 nm. The main features are described in Cinzano (2005 and 2007). The SQM tool and the continuous development of its networks ensure the study and analysis of NSB in the short and long term as described in Bará et al. (2016 and 2019), Ribas et al. (2016), Bertolo et al. (2019), Espey et al. (2014), Posch et al. (2018) and Pun et al. (2012). The growing interest in light pollution and its evolution over time has led to recent in-depth publications on the sensor of this widely used instrument (Fiorentin et al. (2020), (2022) and Bartolomei et al. (2021)). The balloon is also equipped with an external humidity meter. The satellite data used in this paper are acquired from Aqua/MODIS and NPP/VIIRS. Aqua is a polar satellite with an orbit of 708 km of apogee and 691 km of perigee, and the MODIS instrument with which it is equipped observes the earth's surface in 36 spectral bands twice a day. The spectral range used for clouds is between 3.660 and 14.385 μm with spatial resolution of 1 km.
The satellite Suomi National Polar-orbiting Partnership (NPP) equipped with VIIRS has a sun-synchronous orbit of 824 km above the Earth. VIIRS observes atmosphere, land and ocean in the visible and infrared wavelengths: the spectral range of the whisk broom radiometer is between 0.410 and 12.010 μm, divided into 22 channels. VIIRS also observes in a panchromatic Day/Night band (DNB), it is aimed to operate in low-light conditions, and it is ultra-sensitive for the nighttime lights detection. The DNB visible bands have a broad spectral range of $0.5-0.9\mu m$ centred at $0.7\mu m$ and they

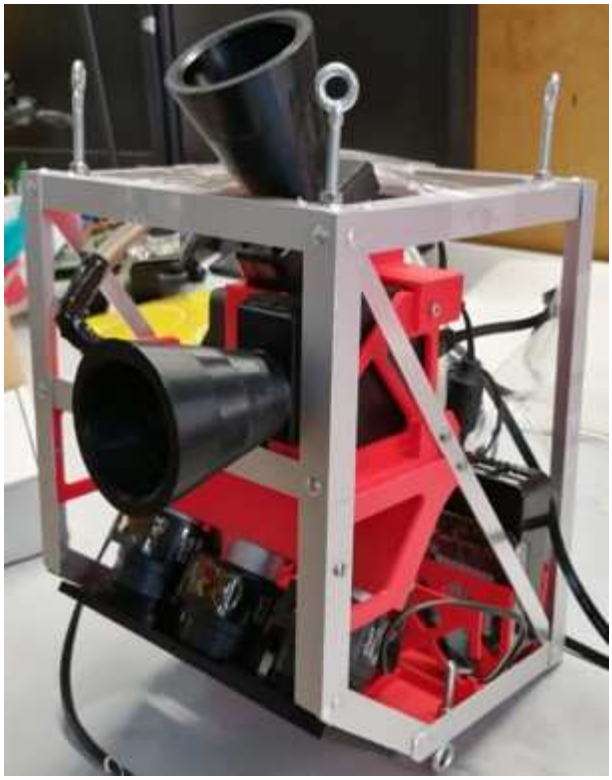

Figure 2. Photo of the SQMs configuration mounted on the light pollution measuring balloon. Black cone limit the field of view of the two SQMs.

have ability to collect low-light imagery at night[1] (Changyong et al., 2017).

Figure 3 shows the 3D reconstruction of the detected VIIRS time averaged radiance in 2021 of the experimental area (left panel). The top right panel shows the 2D map of the balloon's field of view (red polygon). The shape of the polygon depends on the observational geometry in the take-off phase. The Giovanni Interactive Visualization and Analysis Website[2] processes MODIS data. Finally, the monthly average magnitude with a spatial resolution of 742 m in clear sky conditions is acquired by the VIIRS DNB band.

The data will then be used to study the specific contribution of a small town flown over by the balloon: the town of Certaldo (43.54° N, 11.04° E, altitude 70 m, see bottom right panel in Figure 3). The sounding balloon flew over Certaldo after 8.3 minutes at a distance of 7.5 km from the launch point and an altitude of 2000 m. The isolation of this contribution at an altitude of 2000 m provides important information on the propagation of NSB due to ALAN. Finally, MODIS data are used to measure the cloud coverage fraction (CF) and the aerosol optical depth (AOD) (see Figure 4).

[1] https://ncc.nesdis.noaa.gov/documents/documentation/viirs-users-guide-tech-report-142a-v1.3.pdf
[2] https://giovanni.gsfc.nasa.gov

3 UNITS OF MEASUREMENT AND CONVERSIONS

In this Section we make a brief summary of the main units of measurement used and their conversions[3]. The photometric and radiometric quantities used are:

- Luminous flux ϕ, the unit of the luminous flux is lumen (lm). ϕ is defined as the luminous energy emitted, at the wavelength of 555nm, by a point-like monochromatic source, having a luminous intensity equal to a one candela perceived over a solid angle of one steradian.
- Luminous intensity I, is defined as the ratio between the differential luminous flux emitted by the source in a given direction and the solid angle over which it is distributed ($I = \frac{d\phi}{d\omega}$). The unit of measurement of this quantity is the candela (cd); is defined as the light intensity emitted, in a given direction, by a source that emits a monochromatic radiation with a frequency of $540 \cdot 10^{12} Hz$ ($\lambda = 555nm$) and with energy intensity in that direction of $\frac{1}{683}\frac{W}{sr}$.
- Luminance L, of a infinitesimally small surface dS, in a certain direction, is defined through the ratio of the light intensity emitted in a given direction and the projection of the emitting surface on a perpendicular plane to the emission direction. The unit of measurement is the candela per square meter, which is called nit. A light source (primary light source) or an illuminated surface (secondary light source) that emits a certain light intensity in a given direction are characterized by a luminance defined as follows (see Figure 1):

$$L = \frac{d^2\phi}{dS \cdot cos(\theta) \cdot d\omega} = \frac{dI}{dS \cdot cos(\theta)} \left[\frac{cd}{m^2}\right] \quad (1)$$

- Radiance R is a radiometric quantity that describes the amount of electromagnetic emitted radiation reflected (or transmitted) from a surface of unit area, and directed towards a unit solid angle in an indicated direction. In particular, it is used to describe the emission from diffuse sources and the reflection from diffuse surfaces. The SI unit of radiance is Watt per steradian per square meter ($\left[\frac{W}{m^2 \cdot sr}\right]$).

The SQM provides magnitude values M in $\left[\frac{mag}{arcsec^2}\right]$, the VIIRS tool provides radiance R values in $\left[\frac{nW}{cm^2 \cdot sr}\right]$. The conversion formula between radiance and luminance at maximum luminous efficacy ($540 \cdot 10^{12} Hz$, $\lambda = 555nm$) is:

$$\left[\frac{W}{m^2 \cdot sr}\right] = 683 \cdot \left[\frac{cd}{m^2}\right] \quad (2)$$

The general conversion formula is:

$$\phi = K_m \int_{\lambda_{min}}^{\lambda_{max}} \phi(\lambda) V(\lambda) d\lambda \quad (3)$$

in particular $K_m = \frac{683}{V(\lambda)_{max}} \left[\frac{lm}{W}\right] \approx 683 \left[\frac{lm}{W}\right]$, where $V(\lambda)$ is the spectral luminous efficiency for photopic vision and $V(\lambda)_{max} = 1$. We can however use the approximation in Equation 2 considering the aims of this work, the bandwidth of the instruments, and the spatial and temporal resolutions used. This approximation induces an overestimation of the

[3] http://cie.co.at/e-ilv

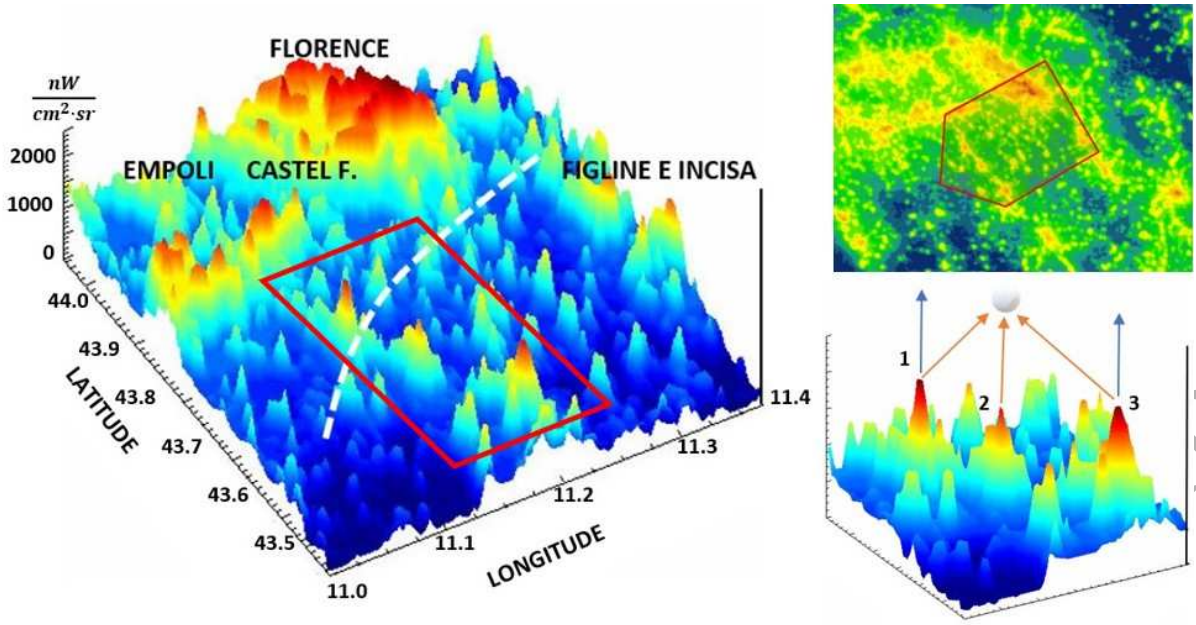

Figure 3. 3D Flight area reconstruction of the annual mean radiance measured by VIIRS (2021, left panel). The top right panel shows the 2D map of the balloon's field of view (red polygon). The bottom right panel shows the zoom of the red rectangle in the 3D map: peak 1 is the town of Castel Fiorentino (17500 inhabitants), peak 2 is the town of Certaldo (16000 inhabitants), peak 3 is the town of Poggibonsi (29000 inhabitants).

radiation obtained by the SQM (Bará et al., 2019), but for the purpose of this publication this is not critical. The conversion formula between luminance and magnitude (Hanel et al., 2018) and the relative inverse formula are:

$$\left[\frac{cd}{m^2}\right] = 10.8 \cdot 10^4 \cdot 10^{-0.4 \cdot \left[\frac{mag}{arcsec^2}\right]} \tag{4}$$

$$\left[\frac{mag}{arcsec^2}\right] = \frac{Log_{10}\left(\left[\frac{cd}{m^2}\right]/10.8 \cdot 10^4\right)}{-0.4}$$

Finally, the formula used to convert SQM data into VIIRS data is:

$$\left[\frac{mag}{arcsec^2}\right] = \frac{Log_{10}\left(\left[\frac{nW}{cm^2 \cdot sr}\right]/7.3764 \cdot 10^{10}\right)}{-0.4} \tag{5}$$

4 EMPIRICAL MATHEMATICAL MODEL OF ALAN PROPAGATION

NSB modeling is a very complex and growing topic. There are sophisticated models that require great computing power and a lot of data (Aubé at al. 2005, 2012, 2014, 2017 and 2018). Our model is simpler and only needs the satellite data described above. It has more limitations than other models, but is useful for preliminary analysis and for the aims of this work. We describe the main assumptions and input-output parameters used. We define the total light radiation emitted in the sky with the summation:

$$\phi_{TOT} = \sum_k \phi_k \left[\epsilon_k + (1-\epsilon_k)\eta_k + (1-\epsilon_k-(1-\epsilon_k)\eta_k)j_k\right] \tag{6}$$

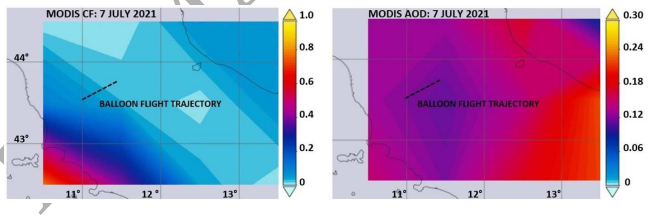

Figure 4. The left panel shows the cloud cover fraction (CF) measured by MODIS during July 7, 2021: $CF < 0.1$ with respect to the flight path of the sounding balloon (dashed line). The right panel shows the aerosol optical depth (AOD) measured by MODIS during July 7, 2021: $0.100 < AOD < 0.200$ in the flight trajectory.

where ϕ_k, ϵ_k, η_k and j_k are respectively the flux emitted by the k-light point, the fraction of scattered light directly above the horizon, the fraction of scattered light and the reflected light fraction in the sky from the illuminated area. Atmospheric scattering grows exponentially with increasing optical path length. The physical principles of the model are described in Cavazzani et al. (2020b). The model works under the hypothesis that Rayleigh scattering is caused by the diffusion of atmospheric molecules, while Mie scattering is caused by the diffusion of aerosols. This assumption, although not always applicable, is functional and effective for our analysis.

The flux per unit area of multiple scattering is treated under the Extended Garstang Model (EGM) assumptions (Cinzano et al., 2012). The multiple scattering mechanism is also treated analytically for all scattering orders in Kocifaj (2018), but the approximations of the EGM are still accurate in this application. The flow per unit of solid angle defines the brightness of the sky due to ALAN:

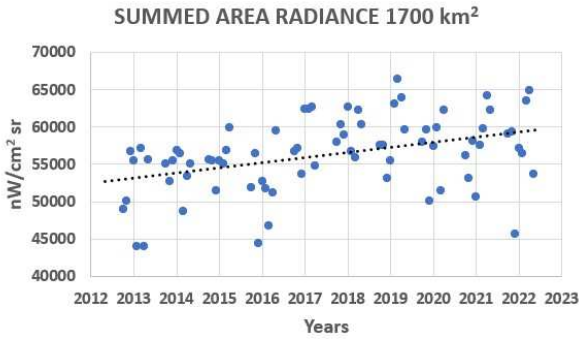

Figure 5. Trend of the summed area radiance measured by VIIRS emitted from the flight area, from September 2012 to April 2022.

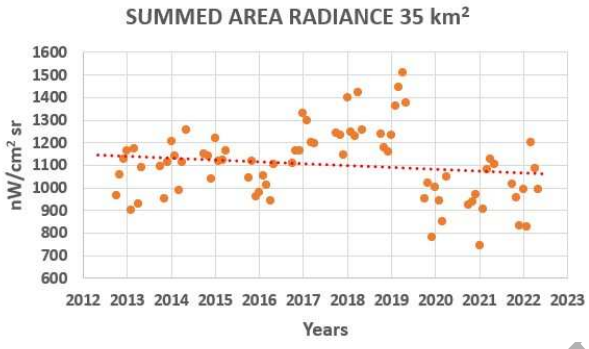

Figure 6. Trend of the summed area radiance measured by VIIRS emitted from the area of the Certaldo town, from September 2012 to April 2022.

Table 1. Table summarizes the model's empirical constants and input parameters. The model provides the calculation of the magnitude as a function of the parameters in column 2.

Empirical constants	Input parameters
$-2.4 < a < -1.8$ (Equation 8)	Population of cities
$0.8 < b < 1.2$ (Equation 8)	Distance and altitude of cities
$0.8 < c < 1.2$ (Equation 10)	Observation interval Δt
$0.5 < d < 1.5$ (Equation 10)	Length of the night Δt_N
$0.5 < f < 1.5$ (Equation 11)	AOD_{Sat}
$0 < A < 1$ (Equation 9)	Aerosol mean radius
$0 < B < 1$ (Equation 11)	$N = \frac{N_{Particles}}{Volume}$
	Molecole mean radius
	Observation wavelength
	Zenith angle
	Altitude of the balloon
Output parameter	Magnitude $\left[\frac{mag}{arcsec^2}\right]$

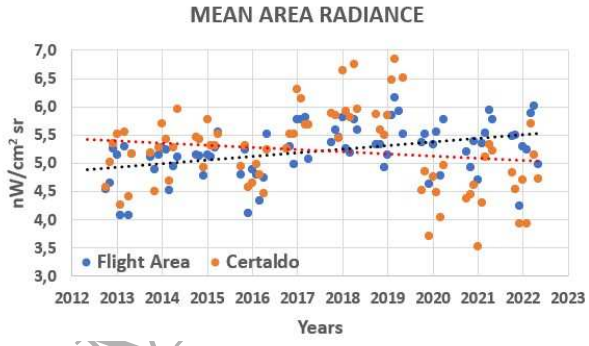

Figure 7. Trend of the mean radiance areas, with their respective linear regressions, measured by VIIRS emitted from the flight area and from the area of the Certaldo town, from September 2012 to April 2022 (blue dots and orange dots respectively).

$$I = \frac{\phi}{\omega}$$

The sky brightness in magnitudes is obtained from the sum of natural and artificial sky brightness:

$$m = constant - 2.5log(I_{Nat} + I_{Art}) \quad (7)$$

Our model is based on the Garstang model (Garstang et al. 1984, 1986, 1989, 1991 and 2007).
Our model is defined through the formula:

$$I = P \times T \times D^{-a} \times MS^{-b} \times E \quad (8)$$

where P and D are respectively the population and the distance. The constants a and b depend on the empirical calibration with respect to the analyzed site (Table 1).
The traffic contribution T is:

$$T = A \cdot P \cdot e^{-\frac{\Delta t}{\Delta t_N}} \sum_{k-light} [\epsilon_k + (1-\epsilon_k)(\eta_k + (1-\eta_k)j_k)] \quad (9)$$

where A is a constant that depends on the observed nation and cities ($0 < A < 1$). Δt is the observation time interval and Δt_N the length of the night.
Multiple scattering (MS) is described by the formula:

$$MS = \frac{N_{Mol}(\theta)n(h)\sigma_{Mol}(\theta)s(h)}{cos^c(\theta)} + \frac{AOD_{Sat}n(h)\sigma_{Aer}(\theta)s(h)}{cos^d(\theta)} \quad (10)$$

where $N = \frac{N_{Particles}}{Volume}$, σ is the cross section, c and d are empirical constants (Table 1). We approximate the vertical distribution of molecules and aerosols n(h) and their size s(h) with exponential decay functions. The extinction factor E is finally defined:

$$E = B \cdot \left(\frac{2\pi\sigma(h)}{\lambda}\right)^f \quad (11)$$

where B varies between $0 < B < 1$ depending on the site and f is an empirical constant (Table 1). All empirical constants are calculated through correlation with SQM data and VIIRS data in relation to the characteristics of the analyzed site.
Table 1 summarizes the input-output parameters of our empirical mathematical model. The model with empirical calibration through satellite data calculates the magnitude as a function of the input parameters described in the Table 1. The use of VIIRS data makes the model applicable to each

site, providing an important preliminary indication on the NSB propagation and its relationship with the AOD, the altitude and the zenith angle.

5 METHODS AND RESULTS

The focus of this work is the novel typology of experimental data. The tool design is finalized for the NSB propagation study through the Earth's atmosphere, obtaining the data presented in the altitude range between 100 m and 12500 m. In this Paper, the SQM data was analyzed in the first hour of flight. During this phase the sounding balloon maintained an average horizontal speed $v_{Hor} = 15m \cdot s^{-1}$ and an average vertical speed $v_{Ver} = 3.8m \cdot s^{-1}$. Figure 3 describes the area overflown by the instrument. The flight is not stabilized, ensuring a 360 degree horizontal field of view. The measurements are taken every second, averaged every minute for correlation with the model. The time interval used for the average therefore includes the NSB north, south, east and west contribution in an altitude range of 230 meters, which is the vertical distance covered in 1 minute by the balloon. Figure 3 shows the 3D reconstruction of the detected VIIRS annual mean radiance in 2021 of the entire experimental area (left panel), from which the trend from September 2012 to April 2022, represented in the Figure 5 is obtained. The bottom right panel in Figure 3 shows the 3D reconstruction of the detected radiance of VIIRS of the Certaldo area, from which the trends (September 2012 to April 2022) represented in the Figure 6 is obtained. Figure 6 shows the trend of the radiance measured by VIIRS from September 2012 to April 2022. Figure 7 shows the average radiance of the two areas that are represented in Figures 5 and 6. The mean area radiance is calculated by dividing the summed area radiance by the number of VIIRS counts in relation to $1700km^2$ and $35km^2$ (e.g. 10788 and 211 counts respectively). The two time series show that all values are between 3.5 and 7.0 $\left[\frac{nW}{cm^2 \cdot sr}\right]$. This means that the average radiance of the entire area is comparable to the average radiance of the Certaldo area.
These values clearly show the effects of the lockdown due to the COVID-19 pandemic as described in the 2021 report: Inquinamento luminoso e lockdown[4]. In fact, we see that in 2020 and 2021 was visible a decrease in radiance from a maximum value of 1500 $\left[\frac{nW}{cm^2 \cdot sr}\right]$ to a minimum value of 750 $\left[\frac{nW}{cm^2 \cdot sr}\right]$ with a maximum range of 750 $\left[\frac{nW}{cm^2 \cdot sr}\right]$ corresponding to a change in magnitude of 0.80 $mag \cdot arcsec^{-2}$ (see Equation 5). Figure 4 shows the cloud cover fraction (CF) mean of the experimental area (left panel). The data refers to a time interval of one hour starting at 23:15 p.m. (UTC) on July 7th, 2021. The cloud fraction is $CF < 0.1$ (left panel), therefore we have a negligible CF or thin veil clouds. The flight was made during a new Moon period: Moon was at 6 percent, and rose at 3:00 a.m. after the conclusion of the experiment. The Moon in combination of aerosols strongly affects NSB (Cavazzani et al. 2020a, 2020b and Puschnig et al., 2020). Figure 4 shows AOD measured by MODIS Terra and Aqua in the experimental area ($0.100 < AOD < 0.200$). We can therefore define the night as completely clear, with low aerosol content and not affected by moonlight. The number of molecules per volume unit is calculated under standard atmosphere conditions: air molar mass $MM = 28.96g$, dry air density $1.225kg \cdot m^{-3}$ at a temperature of $15°C$ and a $1atm$ pressure. The mean molecular radius used is $5 \cdot 10^{-10}m$.
Figure 8 represents the measurement trends of the SQM-V and SQM-H in magnitude (right y-axis), and the humidity trend as a function of altitude (left y-axis). The humidity trend shows the zones of thermal inversion in correspondence with the horizontal sections $1400m < h(m) < 1800m$, and $2200m < h(m) < 3300m$. The trend of the SQM-V measures is significant in the analysis of NSB versus the altitude. We can see a steep rise in the first 300 m (the instrument detects from 18.5 to 21.4 $mag \cdot arcsec^{-2}$). This is caused by two factors: the experimental contamination of the launch area (lighting torches, instrumental setting) and the concentration of aerosols in the first atmospheric layers. These measurements are in accordance with the magnitude values measured by VIIRS between 21.5 $mag{\cdot}arcsec^{-2}$ and 21.8 $mag{\cdot}arcsec^{-2}$ in the hypotheses previously described. These values must be contextualized to the site in question: the value of 21.5 $mag \cdot arcsec^{-2}$ must also be associated with the atmospheric extinction value which consists of scattering and absorption. The magnitude values of 21.5 $mag{\cdot}arcsec^{-2}$ measured cannot be compared to similar values measured in the main ground astronomical sites: e.g. Paranal, La Silla (Cavazzani et al., 2020a), La Palma. This means that a site not contaminated by ALAN but with a high concentration of aerosols at low altitudes could be darker than an astronomical site at high altitude. In fact, atmospheric extinction caused by aerosols and particles that are concentrated in the lower atmosphere blocks the NSB natural component, making the NSB darker at lower altitudes and brighter at higher altitudes.
We can see that all values of SQM-V are between 21.4 $mag \cdot arcsec^{-2}$ and 21.7 $mag \cdot arcsec^{-2}$. This empirically demonstrates that once the 2000 m altitude is exceeded, when the balloon begins to fly over the ALAN sources, the contribution of these sources in the celestial area at 30 degrees from the zenith can be neglected. This could be due to the inverse extinction model (e.g. the main sources come from below and are attenuated at the zenith by the aerosol layers). This interesting experimental result could be due to the presence of black carbon (BC) aerosol, which is the dominant form of light absorbing particulate matter in the atmosphere. The BC aerosol can heat the atmosphere and darken surfaces due to its ability to absorb visible and infrared radiation. These effects have important consequences on the Earth's climate and climate change (Derimian et al., 2008; Ramanathan et al., 2008; and Liu et al., 2020).
The trend of SQM-H measurements shows the greatest variations and therefore more intrinsic information. The fluctuations per second are caused by the rotation of the sounding balloon. The black line in the Figure 8 is the 60 second moving average. This adds up the north, south, west, east contributions of the NSB thanks to the balloon rotation. The trend shows a fall in magnitude from 19.2 to 18.2 $mag{\cdot}arcsec^{-2}$ at an altitude over about $2000m$, corresponding to an increase of 2300 $\left[\frac{nW}{cm^2 \cdot sr}\right]$ due to the overflown Certaldo area (see Equation 5).
Correlation with the model is done by averaging one minute of measurements (see Figure 9). The average constructively exploits the rotation of the balloon by evaluating the north,

[4] https://www.arpa.veneto.it/temi-ambientali/luminosita-del-cielo/file-e-allegati/

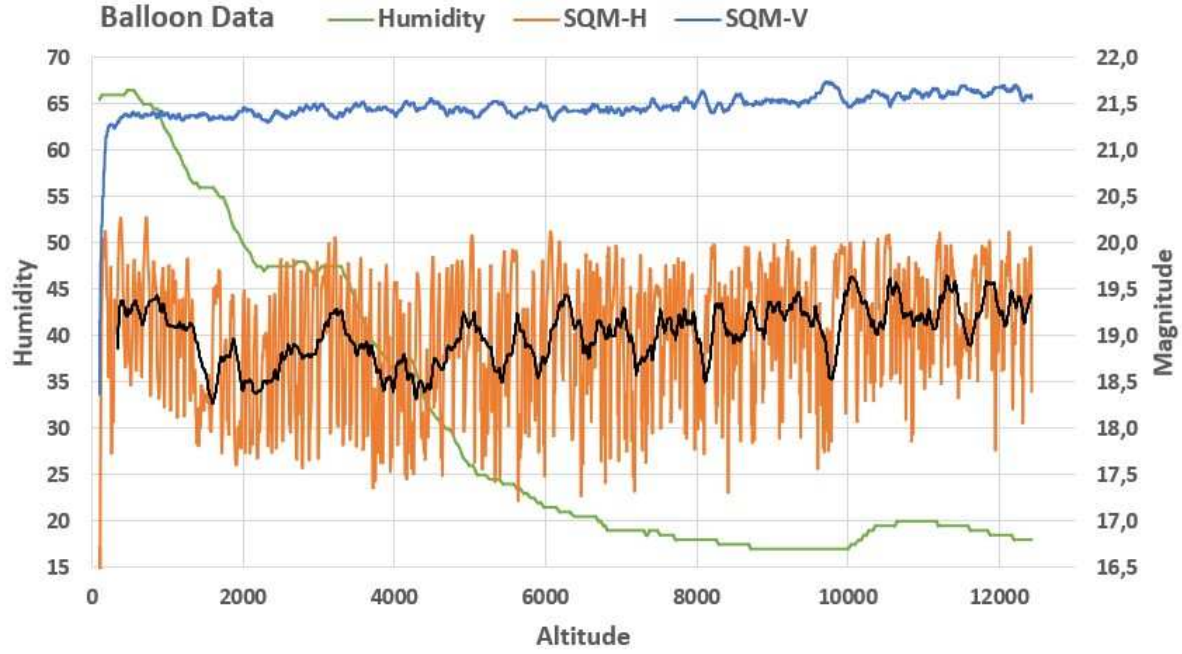

Figure 8. Vertical and horizontal SQM measurements (right y-axis) mounted on the sounding balloon (blue line and orange line respectively) as a function of altitude. The black line represents the one-minute moving average of the SQM-H measurements. The green line shows the external humidity measured by the balloon as a function of altitude (left y-axis).

Table 2. Main cities contributing to ALAN in the experimental area (Tuscany region, Italy). The model assumes an $AOD_{Sat} = 0.1$, particle mean radius $= 1.0\mu m$, zenith angle $= 30°$, observation wavelength $\lambda = 555nm$. The calculated magnitude value from the model is 21.38 at $h(t) = 750m$.

City	P N	T N_1	D(t) $[km]$	h $[m]$	$\Delta h(t)$ $[m]$	AOD	Contribution %
Florence	380000	290000	55	50	700	0.1	20.6
Empoli	48000	3700	34	28	722	0.1	6.2
Castel Fiorentino	17500	1300	30	50	700	0.1	2.8
Certaldo	16000	1200	15	70	680	0.1	9.0
Poggibonsi	29000	2200	13	116	634	0.1	21.4
Tavernelle	7700	600	17	378	372	0.1	3.7
Greve	14000	1100	22	236	514	0.1	4.1
Figline and Incisa	17000	1300	10	122	628	0.1	20.1
Montelupo Fiorentino	14000	1100	30	35	715	0.1	2.3
San Gimignano	8000	610	10	324	426	0.1	9.9
Model NSB $= 21.38 \left[\frac{mag}{arcsec^2}\right]$							

south, east and west contribution of NSB caused by ALAN (zenith angle 90 degrees). The dashed lines represent the two logarithmic trend line of equations:

$$y_{SQM-H} = 0.121 \cdot ln(x) + 18.0 \quad (12)$$

$$y_{SQM-V} = 0.121 \cdot ln(x) + 20.5 \quad (13)$$

This work analyzes in detail the first 10 minutes of the flight in the altitude range between 100 m and 2000 m. Figure 9 clearly shows the take-off phase in an area not contaminated by ALAN, and the rapid decrease in magnitude due to the contribution of the town of Certaldo (16000 inhabitants, altitude 70m, Figure 3). This experimental result allows us to empirically evaluate the contribution in luminance, radiance and magnitude of this area on the horizon at 2000 m altitude, and compare it with the satellite measurement of VIIRS.
Figure 9 shows the comparison between the 1-minute averaged values of the SQM-H (Top panel) and SQM-V (Bottom Panel) used for correlation with the model described in Section 4 (see Figure 10). The model must be implemented in relation to the measures in motion. The use of a one-minute average in the first phase of flight allows to approximate the horizontal and the vertical speeds with two constant values,

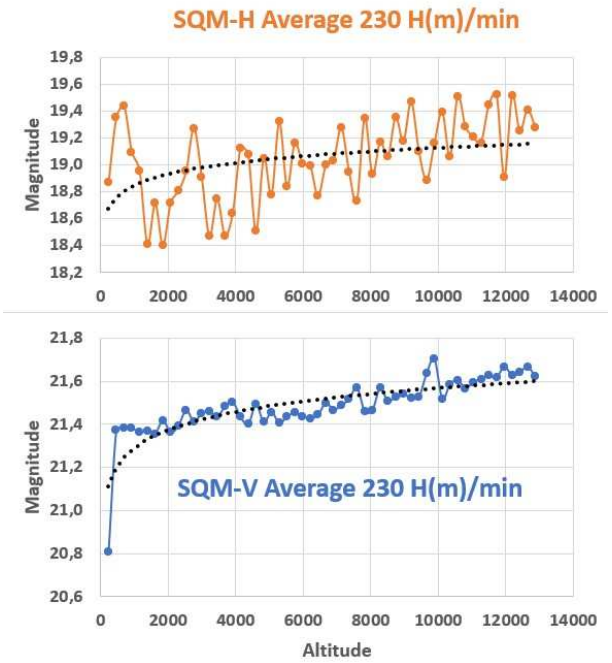

Figure 9. Average of the values of SQM-H (top panel) and SQM-V (bottom panel) for a $\Delta t = 1$ minute corresponding to an $\Delta h = 230m$. The dashed lines represent a logarithmic trend line.

obtaining the distance from the main sources of ALAN following hourly law:

$$\vec{D_x}(t) = \vec{D_0} + \vec{v_{x,0}} \cdot t \tag{14}$$

Altitude must also be related to time:

$$\vec{h_z}(t) = \vec{h_0} + \vec{v_{z,0}} \cdot t \tag{15}$$

The code then calculates the distance and altitude every minute by evaluating the magnitude value. Table 2 shows the values between the second and third minute (SQM-V, zenith angle 30 degrees) after launch to exclude the contamination of the take-off area and overcome the first aerosol layers. The Pearson correlation between the values shown in Figure 9 and the model is 85 percent for SQM-H and 91 percent for SQM-V (see Figure 10). The correlation value provides an estimate of the model's percentage error: horizontal error $\delta_H = 15$ percent and vertical error $\delta_V = 9.0$ percent. The angle of view of an SQM-L is 20 degrees, so SQM-V will measure between $20° \leqslant z \leqslant 40°$ while SQM-H will observe between $80° \leqslant z \leqslant 100°$. The lowest correlation model-SQM-H depends on this angle of view. A zenith angle of 100 degrees corresponds to an angle of -10 degrees below the horizon. This implies a direct component from the ALAN source. The model works between $0° < z < 90°$ degrees and is not valid for larger angles. This induces a systematic error that underestimates the radiance emitted by the ALAN sources.

6 DISCUSSION AND CONCLUSION

In this work we describe the results of an innovative experiment for the study of NSB with particular attention to the

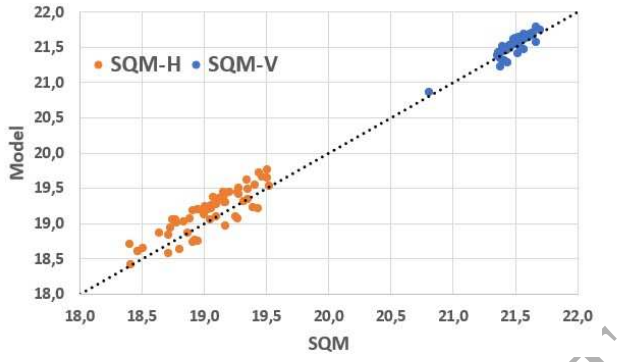

Figure 10. Correlation between the mean value of the measurements of SQM-H (0.85) and SQM-V (0.91) for a $\Delta t = 1$ minute corresponding to an $\Delta h = 230m$ (x axis) and the model (y axis). The dashed line represents the quadrant bisector.

sources of ALAN (Figure 1). The publication of the original data collected in relation to the astronomical observation and propagation of NSB empirically shows the dependence to altitude and humidity (Figure 8). We compare the measurements obtained with the VIIRS satellite data (Figure 3) in relation to the atmospheric conditions detected by the MODIS satellite data (Figure 4). In Section 3 we describe the main photometric and radiometric quantities and the respective conversion formulas to make comparisons between measurements. In particular, we analyze the first part of the flight to isolate the contribution of the Certaldo area (bottom right panel in Figure 3) detected by the sounding balloon at an altitude of 2000 m. The important empirical result, subsequently modeled in correlation with the model described in Section 4, shows that at the zenith this ALAN contribution at an altitude greater than 2000 m is negligible. Figure 8 shows the NSB trend as a function of altitude. The take-off phase shows a rapid increase in the magnitude measured by the SQM-V, this could be related to the concentration and type of aerosol present in the lower atmospheric layers (Sciezor and Czaplicka, 2020; Kocifaj and Bará, 2021). The flight of the sounding balloon is conducted in optimal conditions over the experimental area for $AOD \approx 0.1$, clear sky and moonless conditions. The measurements of SQM-H and SQM-V under these assumptions are averaged over one minute. This averages the contribution of north, south, west, east, thanks to the rotation of the balloon, for a vertical drop of 230 m (Figure 9). In the first phase of flight, we can in fact assume constant horizontal and vertical speeds. These means are used for the correlation described in Figure 10: the Pearson correlation between the values and the model is 85 percent for SQM-H and 91 percent for SQM-V. The experimental evidence, supported by theoretical modeling, of the strong dependence between altitude and ALAN contamination of the NSB is fundamental for the analysis of important astronomical sites or for new site testing campaigns. Altitude also strongly affects the concentration and size of aerosols. Aerosols are the atmospheric components responsible for the propagation of NSB through scattering. The use of sounding balloons for astronomical purposes is known, but the configuration of these for the NSB measurement is an important novelty with broad prospectives for scientific research. The results described in this work can offer useful indications for

the preservation of important astronomical sites, the choice of new sites and all the related multidisciplinary implications.

6.1 ACKNOWLEDGMENTS

This activity is supported by the INAF (Istituto Nazionale di Astrofisica) funds allocated to the Premiale ADONI MIUR. MODIS data were provided by the *Giovanni - Interactive Visualization and Analysis* website. We also refer to the 3D atmospheric reconstruction project at Prato Piazza (Italy). Funding from Italian Ministry of Education, University and Research (MIUR) through the *Dipartimenti di eccellenza project Science of the Universe*. We thank the anonymous referee for useful advice and interesting insights.

6.2 Data availability

A part of the data underlying this paper will be shared on reasonable request to the corresponding author while a part of the data are available as described in the paper footnote.

REFERENCES

Aubé M., Franchomme-Foss L., Robert-Staehler P., Houle V., 2005, Light t' pollution modelling and detection in a heterogeneous environment: toward a night-time aerosol optical depth retreival method. Optics and Photonics 2005, International Society for Optics and Photonics, p. 589012

Aubé, M., Kocifaj, M., 2012, MNRAS, 422, 819

Aubé M., Fortin N., Turcotte S., Garcia B., Mancilla A., Maya J., 2014, PASP, 126, 1068

Aubé M., Simoneau A., 2017, Illumina UserŠs Guide, Available at: https://w1. cegepsherbrooke.qc.ca/ aubema/index.php/Prof/IlluminaGuide2016

Aubé M., Simoneau A., 2018, t' J. Quant. Spectrosc. Radiat. Transfer, 211, 25

Aubrecht C, Jaiteh M, De Sherbinin A., 2010, Global assessment of light pollution impact on protected areas. New York: Columbia University, 6Ű7

Bará, S.,2016, R. Soc. Open Sci., 3, 160541

Bará, S., Lima R.C., Zamorano J., 2019, Sustainability, 11, 3070

Bará, S., Tapia, C.E. and Zamorano, J., 2019, Sensors, 19(6), 1336; https://doi.org/10.3390/s19061336

Bartolomei, M., Olivieri, L., Bettanini, C., Cavazzani, S., Fiorentin, P., 2021, Sensors, 21, 22, 7544

Bertolo, A., Binotto, R., Ortolani, S., Sapienza, S., 2019, J. Imaging, 5, 56

Bettanini, C., Bartolomei, M., Aboudan, A., Colombatti, G., Olivieri, L., 2022, Acta Astronautica, 191, 11-21

Cabrera-Cruz, S. A., Smolinsky J. A., Buler J., 2018, Scientific Reports, 8, 3261

Cavazzani, S., Ortolani, S., Zitelli, V., 2012, MNRAS, 419, 3081

Cavazzani, S., Zitelli, V., 2013, MNRAS, 429, 1849

Cavazzani, S., Ortolani, S., Zitelli, V., 2015, MNRAS, 452, 2185

Cavazzani, S., Ortolani, S., Zitelli, V., 2017, MNRAS, 471, 2616

Cavazzani, S., Ortolani, S., Scafetta, N., Zitelli, V., Carraro, G., 2019, MNRAS, 484, L136ŰL140

Cavazzani, S., Ortolani, S., Bertolo, A., Binotto, R., Fiorentin, P., Carraro, G., Saviane, I., Zitelli, V., 2020, MNRAS, Volume 493, 2463Ű2471

Cavazzani, S., Ortolani, S., Bertolo, A., Binotto, R., Fiorentin, P., Carraro, G., Zitelli, V., 2020, MNRAS, Volume 499, 5075Ű5089

Changyong, C., Wenhui, W., Slawomir, B., Bin, Z., 2017, JGR Atmospheres, Vol. 122, 5285

Cinzano, P., 2005, ISTIL Intern. Rep., 9, v. 1.4.

Cinzano, P., 2007, ISTIL Internal Report., available at: http://unihedron.com/projects/sqm-l/sqmreport2.pdf

Cinzano, P., Falchi, F., 2012, MNRAS, 427, 3337

Derimian, Y., Karnieli, A., Kaufman, Y. J., Andreae, M. O., Andreae, T. W., Dubovik, O., Maenhaut, W., and Koren, I., 2008, Atmos. Chem. Phys., 8, 3623Ű3637

Espey, B., McCauley, J., 2014, Light. Res. Technol., 46, 67-77

Fiorentin, P., Bettanini, C., Bogoni, D., 2019, Sensors, 19(23), 5091

Fiorentin, P., Bertolo, A., Cavazzani, S., Ortolani, S., 2020, Journal of Quantitative Spectroscopy and Radiative Transfer, 255, 107235

Fiorentin, P., Cavazzani, S., Ortolani, S., Bertolo, A., Binotto, R., 2022, Measurement, 191, 110823

Garstang, R. H., 1984, Observatory, 104, 196

Garstang, R. H., 1986, PASP, 98, 364

Garstang R. H., 1989a, PASP, 101, 306

Garstang R. H., 1991, PASP, 103, 1109

Garstang, R. H., 2007, The Observatory, Vol. 127, No. 1, p. 1-13

Gaston, K., Bennie, J., Davies, T.W., Hopkins, J., 2013, Biol. Rev., 88, 912Ű927

Haim A, Zubidat AE., 2015, Philos Trans R Soc., 370

Hanel, A., Posch, T., Ribas, S.J., Aubé, M., Duriscoe, D., Jechow, A., Kollàth, Z., Lolkema, D.E., Moore, C., Schmidt, N., et al., 2018, J. Quant. Spectrosc. Radiat. Transf., 205, 278-290

Holker, F., Wolter, C., Perkin, E., Tockner, K., 2010, Trends in Ecology and Evolution, 25, 681-682

Horvath, H., 2014, Journal of Quantitative Spectroscopy and Radiative Transfer, Vol. 139, 3-12

Kloog, I., Haim, A., Stevens R.G., Portnov, B.A., 2009, Chronobiology International, 26, 108-125

Kocifaj, M., 2018, Journal of Quantitative Spectroscopy and Radiative Transfer, Vol. 206, 260-272

Kocifaj, M., Salvador Bará, 2021, MNRAS, Letters, 500, 1, L47ŰL51

Kyba, C., Tong, K., Bennie, J. et al., 2015, Worldwide variations in artificial skyglow, Sci Rep 5, 8409 (2015) doi:10.1038/srep08409

Liu, D., He, C., Schwarz, J.P. et al., 2020, npj Clim Atmos Sci 3, 40

Manfrin, A., Singer, G., Larsen, S., Wei, N., et al., 2017, Front. Environ. Sci, DOI:10.3389/fenvs.2017.00061

Mulder, C., Bennett, E.M., Bohan, D.A., Bonkowski, M., Carpenter, S.R., Chalmers, R., Cramer, W., Durance et al., 2015, Advances in Ecological Research, Vol. 53, 1-53

Patat, F., 2008, Astronomy and Astrophysics, 481, 575

Posch, T., Binder, F., Puschnig, J., 2018, J. Quant. Spectrosc. Radiat. Transf., 211, 144-165

Pun, C.S.J., So, C.W., 2012, Environ. Monit. Assess., 184, 2537-2557

Puschnig, J., Posch, T., Uttenthaler, S., 2014, J. Quant. Spectrosc. Radiat. Transf., 139, 64-75

Puschnig, J., Wallner, S., Posch, T., 2020, MNRAS, 492, 2622

Ramanathan, V., Carmichael, G., 2008, Nature Geosci 1, 221Ű227

Ribas, S. J., Torra, J., Figueras, F., Paricio, S., Canal-Domingo, R., 2016, Int. J. Sustainable Lighting, 35, 32Ű36

Schernhammer ES, Laden F, Speizer FE, et al., 2001, J Natl Cancer Inst., 93, 1563Ű1568

Shiraiwa M., Ueda K., Pozzer A., Lammel G., Kampf C.J., Fushimi A., Enami S., Arangio A.M. et al., 2017, Environ. Sci. Technol., 51, 23, 13545Ű13567

Sciezor, T. and Czaplicka, A., 2020, Journal of Quantitative Spectroscopy and Radiative Transfer. 254. 107168

Stevens, R.G., Brainard, G.C., Blask, D.E., Lockley, S.W., Motta, M.E., 2013, AJPM, 45, 343-346

Walker, W.H., Walton, J.C., DeVries, A.C., Nelson, R.J., 2020, Transl. Psychiatry 2020, 10

Walker, W.H.; Borniger, J.C.; Gaudier-Diaz, M.M.; Hecmarie

Melendez-Fernández, O.; Pascoe, J.L.; Courtney DeVries, A.; Nelson, R.J., 2020, Mol. Psychiatry , 25, 1080Ű1093

Walker, W.H., Bumgarner, J.R., Walton, J.C., Liu, J.A., Melendez-Fernández, H., Nelson, R.J. and DeVries, A.C., 2020, Int. J. Mol. Sci., 21(24), 9360, https://doi.org/10.3390/ijms21249360

Yang, W.S., Wang, X., Deng, Q., Zhao, H. and Fan, W.Y., 2015, Br J Cancer, 112(11), 1838Ű1839

Zhang, J., Fan, Z., Yan, J., Kumar, Y.B., Hong-Bin Li et al., 2016, Publications of the Astronomical Society of the Pacific Vol. 128, pp. 1-6